Acta Materialia 130 (2017) 361–374

Contents lists available at ScienceDirect

Acta Materialia

journal homepage: www.elsevier.com/locate/actamat

Full length article

On the breakaway oxidation of Fe9Cr1Mo steel in high pressure CO_2

Y. Gong [a], D.J. Young [c], P. Kontis [a], Y.L. Chiu [d], H. Larsson [e, f], A. Shin [g], J.M. Pearson [g], M.P. Moody [a], R.C. Reed [a, b, *]

[a] Department of Materials, University of Oxford, Parks Road, Oxford OX1 3PH, United Kingdom
[b] Department of Engineering Science, University of Oxford, Parks Road, Oxford OX1 3PJ, United Kingdom
[c] University of New South Wales, 2052 Sydney, NSW, Australia
[d] School of Metallurgy and Materials, University of Birmingham, Edgbaston, Birmingham B15 2TT, United Kingdom
[e] Unit of Structures, Department of Materials Science and Engineering, KTH Royal Institute of Technology, SE-10044 Stockholm, Sweden
[f] Thermo-Calc Software AB, Råsundavägen 18, SE-169 67 Solna, Sweden
[g] EDF Energy Generation, Barnwood, UK

ARTICLE INFO

Article history:
Received 15 November 2016
Received in revised form
1 February 2017
Accepted 12 February 2017
Available online 16 February 2017

Keywords:
Oxidation
Carburisation
Breakaway
Characterisation
Modelling

ABSTRACT

Fundamental insights into the mechanism of breakaway oxidation in Fe9Cr1Mo steel are deduced, through advanced characterisation and modelling. Degradation at 600 °C/~42 bar CO_2 for ~20,000 h is emphasised: conditions relevant to components such as the finned superheater tubes used for advanced gas-cooled nuclear reactors. It is shown that such conditions are sufficient to cause carbon saturation of the metallic substrate, as confirmed by direct observation of extensive carbide precipitation but also numerical analysis of the carbon transport. Thus the observation of graphite precipitation close to the scale/metal interface is rationalised. Nonetheless, the activity of carbon at the scale/metal interface does not reach unity – with respect to graphite – at time zero. A modelling method is proposed which accounts for this kinetic retardation of the attack; this can be used to interpolate across the regimes within which breakaway oxidation is prevalent. It is a plausible model for extrapolation to the lower temperatures relevant to service conditions and is suitable for lifetime estimation – so-called 'remnant life analysis' – of such safety-critical components when prone to this form of attack.

1. Introduction

Ferritic-martensitic 9Cr steels (P91, P92) possess good creep strength and adequate corrosion resistance in CO_2 environments at medium temperatures (400–700 °C). An important application is in CO_2 gas-cooled nuclear reactors, typically in the temperature range 480–520 °C [1]. Corrosive attack in these circumstances is characterised by an outer, duplex scale consisting of magnetite and Cr-rich spinel layers, accompanied by precipitation of Cr-rich carbides within the underlying steel [2]. Whilst the kinetics are close to parabolic at first, increasing carburisation leads to the onset of rapid linear kinetics. This 'breakaway' corrosion phenomenon is of practical significance, as it limits reactor lifetimes. It is also of fundamental significance, as the processes whereby a low carbon activity gas can carburise steels and ultimately produce graphite which mechanically disrupt the protective scale and potentially triggers the 'breakaway' kinetics are not well understood [3–5].

Prediction of the time needed for breakaway effect is of significant fundamental interest but also practical importance, since breakaway attack is aggressive: it results in significant loss of metal cross-section very quickly. Use can be made of long term accelerated tests at higher temperatures – 580–640 °C for example – to quantify the time for breakaway, but then one needs to identify the most appropriate means of extrapolation to service conditions for the purposes of the determination of component life [6]. Ideally, physics-based approaches rather than statistical means are preferred, but these do not exist as yet. Interestingly, the exact details of the rate-controlling steps leading to the 'breakaway' oxidation are still under considerable discussion and are controversial [7–11]. Quantitative numerical modelling is needed to address this situation, with the additional advantage of the possibility of a physics-based approach to the prediction of the reaction kinetics as a function of temperature.

In this paper, Fe9Cr1Mo steel at/close to the point of breakaway is first characterised using modern analytical techniques in order to

* Corresponding author. Department of Materials, University of Oxford, Parks Road, Oxford OX1 3PH, United Kingdom.
E-mail address: roger.reed@eng.ox.ac.uk (R.C. Reed).

http://dx.doi.org/10.1016/j.actamat.2017.02.034

better understand the degradation mechanisms occurring. The observations are rationalised using thermodynamic and kinetic modelling. Calculations are carried out to compare the predicted rate of carbon uptake with that deduced by experiment – it is concluded that some form of surface-limited reaction causes a delay in carbon uptake. Numerical modelling is used to describe the approach of the metal substrate to carbon saturation, on the assumption that breakaway oxidation is associated with it. Predictions are made of the fraction of the mass gain associated with (i) oxidation and (ii) carburisation, assuming that no carbon can dissolve in the oxide scale. Finally, a method is proposed to allow for the extrapolation of the time to breakaway data from higher to lower temperatures, which will be of significant practical value.

2. Experimental procedures

The material considered is Fe-9Cr1Mo steel of production-grade quality, see Table 1. The 3D geometry of the specimen considered is shown in Fig. 1(a). Autoclaves (inner volume of ~22.5 l) were used to degrade the material at a gas pressure of 600 psig (42.38 bar), gas composition of 100 vppm H_2, 300 vppm CH_4, 1 vol% CO, 300 vppm H_2O and balance CO_2 and gas flow rate of 20 cc/min at standard temperature and pressure (STP). Four temperatures – 580, 600, 620 and 640 °C – were employed above the temperature of operation, to encourage accelerated breakaway. Fig. 2 shows estimates for equilibrium oxygen activity (a_O) and carbon activity (a_C) for these conditions between 400 and 700 °C; Gibbs-energy minimisation was conducted using Thermo-Calc 2015b with SGTE Substances Database 5.1 including all assessed gaseous species. The a_O is predicted to be in the range 5×10^{-24}–10^{-21} and a_C between 0.02 and 0.1. Specimen manufacture, autoclave operation and specimen examination were conducted by Amec Foster Wheeler on behalf of EDF Energy.

The exposure intervals were between 250 h and 5 kh, shorter exposure intervals being used at higher temperatures. The time to breakaway (TTB) was taken to be the exposure time at the moment of breakaway, as first observed on the fin tip of the samples; the weight gain at breakaway (WGB) was (conservatively) taken to be the weight gain observed immediately prior to visual observation of breakaway initiation. The mass gain data are summarised in Fig. 3: higher temperatures give larger weight gains but lower TTB; moreover the weight gain data exhibit more scatter as breakaway initiation is approached, suggesting large variance of TTB/WGB and post-breakaway kinetics.

A specimen exposed to 600 °C was chosen for detailed high-resolution microstructural characterisation, since a transition between protective/breakaway oxidation was observed, see Fig. 1(b); the specimen was exposed for 19,924 h while the first breakaway initiation of two fins was observed at 18,921 h. Thus the degree of degradation in the right hand fin can be assumed to approach that needed to initiate breakaway. A JEOL 6500F field emission gun scanning electron microscope (FEG-SEM) in backscattered electron imaging mode was used. In addition, energy dispersive X-Ray (EDX) chemical mapping was conducted at the internal oxide zone (IOZ) using a Zeiss Merlin FEG-SEM, with a beam of 5 keV energy and a probe current of 500 pA.

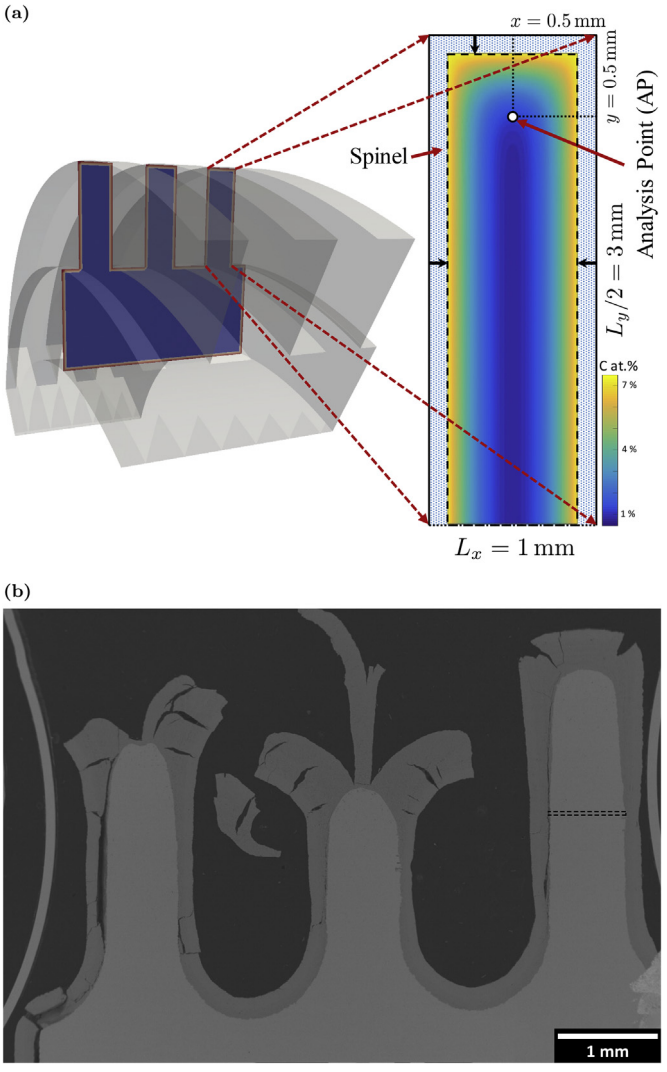

Fig. 1. (a) Illustration of the geometry of the fin tube specimen (left) with assumed fin dimension for life assessment as described in § 6.3 (right); (b) Backscattered SEM image of the cross-section of the fin tube exposed at 600 °C for 19,924 h. Note the right fin is just before breakaway initiation and the other two fins are during breakaway oxidation; measured profile of carbide volume fraction in black box region on the right fin is shown in Fig. 8.

For site-specific analysis, samples were prepared for transmission electron microscopy (TEM) and atom probe tomography (APT) using a FEI Quanta 3D FEG FIB/SEM and an NVision 40 dual beam FIB, respectively, following [12]. The TEM studies were carried out on a Talos F200 S/TEM operating at 200 keV. A Super-X EDS system with four silicon drift detectors (SDD) is integrated in the S-TWIN lens and offers the solid angle of 0.9 sr. Atom probe analysis was performed in a Cameca LEAP 3000X HR instrument operating in laser mode with pulse rate at 200 kHz and pulse energy at 0.4 nJ.

Table 1
Measured composition of steel (wt.%); carbon and sulphur are measured by the combustion analysis while the rest by the Inductively Coupled Plasma Optical Emission Spectometry (ICPOES).

C	Co	Cr	Cu	Fe	Mn	Mo	Nb	Ni	P	S	Si	Ti	V	W
0.093	0.02	9.20	0.16	Bal.	0.47	1.04	<0.02	0.21	0.011	0.008	0.67	<0.02	<0.05	<0.05

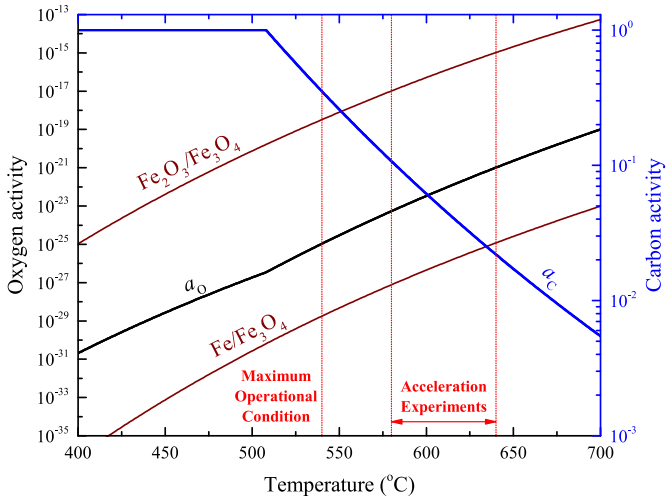

Fig. 2. Thermodynamic predictions of equilibrium activities of oxygen (black) and carbon (blue) for exposure gas condition (300 vppm H_2O, 100 vppm H_2, 300 vppm CH_4, 1 vol% CO and balance CO_2) at pressure of 600 psig (42.38 bar); equilibrium oxygen activities for typical iron oxides (brown); calculations were conducted using Thermo-Calc 2015b with SGTE Substances Database 5.1. (For interpretation of the references to colour in this figure legend, the reader is referred to the web version of this article.)

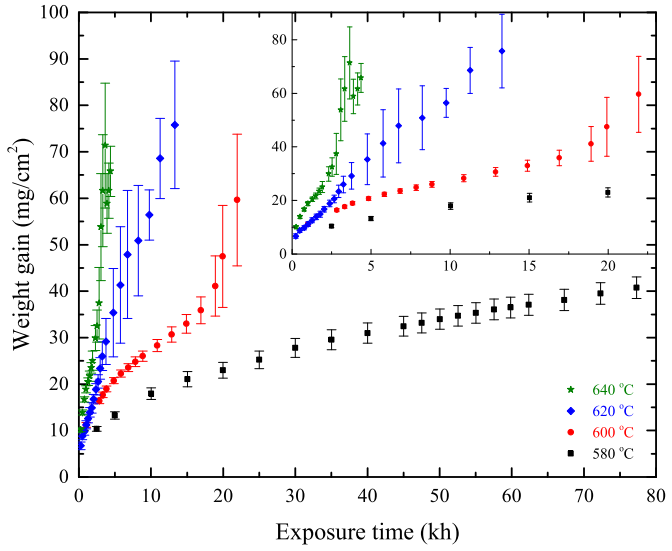

Fig. 3. Weight gain changes of experimental samples exposed at 580 °C (black), 600 °C (red), 620 °C (blue) and 640 °C (green) with gas compositions of 100 vppm H_2, 300 vppm CH_4, 1 vol% CO, 300 vppm H_2O and balance CO_2 at gas pressure of 600 psig (42.38 bar); one stand deviation from repeated tests is used to evaluate uncertainties. (For interpretation of the references to colour in this figure legend, the reader is referred to the web version of this article.)

3. Theoretical modelling

In what follows, we deal first with the kinetics of outer scale formation, in what is termed an oxide growth model (OGM). Second, we perform coupled thermodynamic/kinetic calculations in 1D using the DiCTra code and an associated homogenisation model. Finally, consideration is given to the modelling of carbon uptake in 2D in what is termed a substrate penetration model (SPM).

3.1. Oxide growth model (OGM)

The oxide growth model (OGM) is illustrated in Fig. 4. As shown by inert marker experiments [13] iron diffuses outward to form the outer Fe_3O_4 layer, and the spinel layer grows inward. Solid-state diffusion of oxygen is far too slow to support the latter process [14], and another, faster process is in effect. The observation that the inner layer is porous has led to the proposal of gas phase molecular transport as part of the available space model [15,16]. Partial pressures of O_2 within the scale are too low to provide sufficient mass transport. Instead, this role is filled by CO_2, as evidenced by $C^{18}O_2$ tracer experiments [17] and the simultaneous carburisation of the steel.

Inward transport of CO_2 is not explicitly treated in the available space model, but has been recognised [10] as a diffusion controlled process. It is clear that a large gradient in CO_2 fugacity is maintained across the spinel layer (a) to allow local equilibrium with the oxygen activity profile, and (b) to account for the observed carburisation of the steel (a large value of P_{CO_2} would cause its decarburisation). Accordingly, we propose that CO_2 transports via the gas phase within pores, but also via grain boundaries within the oxide separating the pores. It is this process which supports both oxide scaling and alloy carburisation.

The flux balance at the spinel/alloy interface can be written:

$$\upsilon_{sp}\left(C_O^{alloy} - C_O^{sp}\right) = J_O^{alloy} - J_O^{sp} \tag{1}$$

where υ_{sp} is the velocity of the spinel/alloy interface measured relative to the original alloy/gas interface. The terms C_i^k and J_i^k are the interfacial concentrations and interfacial fluxes in a volume-fixed frame of reference of component i in phase k, respectively. Note that the C_i^k are, here, evaluated as u_i^k/V_m where V_m is the molar volume and u_i^k are the u-fractions which can be evaluated readily from the mole fractions x_i^k, consistent with

$$u_i^k = \frac{x_i^k}{\sum\limits_{j\in S} x_j^k} \tag{2}$$

Note that by $j \in S$ one should infer that the summation is taken over the substitutional components only. Assuming negligible solubility of oxygen in the alloy and thus zero flux, Equation (1) reduces to

$$\upsilon_{sp} = \frac{J_O^{sp}}{C_O^{sp}} \tag{3}$$

where υ_{sp} can then be used to estimate the spinel thickness X_{sp} via:

$$X_{sp} = \int_0^t \upsilon_{sp}\, dt \tag{4}$$

and J_O^{sp} depends on the thermodynamic driving force and effective mobilities. Assuming the linearised gradient approximation, one has:

$$J_O^{sp} \simeq J_O^{sp'} = -M_O C_O^{sp} \frac{\mu_O^{sp/alloy} - \mu_O^{mag/sp}}{X_{sp}} (1 - f_{SiO_2}) \tag{5}$$

where $J_O^{sp'}$, M_O, X and the μ denote the interfacial flux in a lattice-fixed frame of reference, the effective mobility of oxygen (as CO_2), oxide thickness and interfacial chemical potentials, respectively. Diffusional blocking by silica formed near the spinel/alloy interface [18] is explicitly recognised, and f_{SiO_2} is the fraction of spinel/alloy interface across which diffusion is blocked in this way. The diffusion length is taken as X_{sp} and

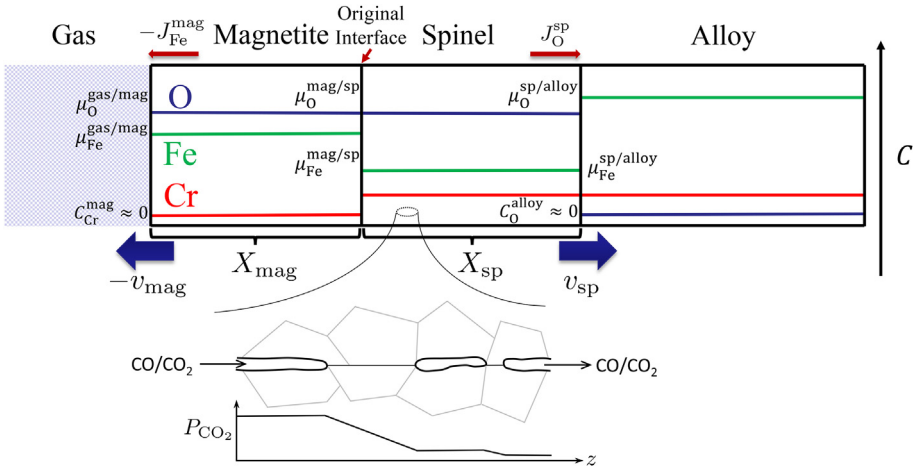

Fig. 4. Illustration of the oxide growth model (OGM) with defined physical parameters annotated. Inset shows proposed model for oxygen and carbon transport, involving gas phase mass transport within pores, and grain boundary diffusion between them.

$$\mu_O^{mag/sp} \simeq \mu_O^{gas/mag} \tag{6}$$

as the oxidation kinetics are dominated by the inner spinel layer; this assumption is supported by the negligible effect on the re-oxidation rate of the removal of the outer magnetite layer [19].

As Si diffusion is relatively slow in ferrite (its chemical diffusivity is less than 10^{-18} m^2/s at 640 °C, see Ref. [20]), it is assumed that the amount of SiO_2 accumulated at the interface (mole per unit spinel/alloy surface area), n_{SiO_2}, is proportional to X_{sp}, as the inward growth of a spinel layer X_{sp} thick corresponds to consumption of an alloy zone of the same thickness. Hence

$$n_{SiO_2} = C_{Si} X_{sp} \tag{7}$$

where C_{Si} is the alloy concentration of Si. Assuming further that f_{SiO_2} is proportional to n_{SiO_2}, one has:

$$f_{SiO_2} = sC_{Si}X_{sp} \tag{8}$$

where s[m^2 mol^{-1}] is now termed the SiO_2 blocking factor. Equations (3)–(8) give the following implicit expression for X_{sp}

$$\exp\left\{sC_{Si}\left[\left(\mu_O^{sp/alloy} - \mu_O^{gas/mag}\right)sC_{Si}M_O t - X_{sp}\right]\right\} + sC_{Si}X_{sp} = 1 \tag{9}$$

Finally, by considering the flux of iron at the gas/magnetite interface – and using the same approximations as above – the following equations are obtained:

$$v_{mag} = \frac{J_{Fe}^{mag}}{C_{Fe}^{mag}} \tag{10}$$

$$J_{Fe}^{mag} \simeq J_{Fe}^{mag'} = -M_{Fe}C_{Fe}\frac{\mu_{Fe}^{sp/alloy} - \mu_{Fe}^{mag/sp}}{X_{sp}}(1 - f_{SiO_2}) \tag{11}$$

$$\mu_{Fe}^{mag/sp} \simeq \mu_{Fe}^{gas/mag} \tag{12}$$

$$X_{mag} = -\int_0^t (v_{mag} + v_{sp})\, dt \tag{13}$$

yielding:

$$X_{mag} = -X_{sp}\left(\frac{\left(\mu_{Fe}^{sp/alloy} - \mu_{Fe}^{gas/mag}\right)M_{Fe}}{\left(\mu_O^{sp/alloy} - \mu_O^{gas/mag}\right)M_O} + 1\right) \tag{14}$$

Both M_{Fe} and M_O are written

$$M_k = \frac{M_k^\circ}{RT}\exp\left(\frac{-Q_k}{RT}\right) \tag{15}$$

Neither the activation energy nor the pre-exponential factor is known for iron or oxygen, because the microstructure of the spinel layer is not quantitatively defined, although the material is clearly fine-grained and porous. For this reason, the mobilities are treated as adjustable quantities in optimising the description of observed scaling rates.

3.2. DiCTra simulations

To complement the above, the homogenisation model [21,22] implemented in the 1D DiCTra diffusion code has been used to evaluate the phase evolution and diffusion within the underlying ferritic substrate in 1D. Note that no attempt has been made to account for transport through the oxide scale; instead boundary conditions for oxygen and carbon are assumed to apply at the scale/metal interface. Version 2015b of the DiCTra code has been used, in conjunction with the thermodynamic database TCFE8 from Thermo-Calc. If any correlation effects of successive atom-vacancy jumps and all other kinetic and thermodynamic cross-effects are ignored, the flux of an element k[mol m^{-2} s^{-1}] in the single phase region along spatial coordinate z in the lattice-fixed frame of reference can be modelled as:

$$J_k = -M_k C_k \frac{\partial \mu_k}{\partial z} \tag{16}$$

with continuity maintained consistent with:

$$\frac{\partial C_k}{\partial t} = \frac{\partial}{\partial z}(-J_k) \tag{17}$$

With the homogenisation model, multi-component diffusion is modelled by assuming that at each point along the reaction front the local phase assemblage comes to local equilibrium, consistent with the local equilibrium assumption. The transport properties of component k within each phase ϕ are defined by:

$$\Gamma_k^{\phi} = M_k^{\phi} C_k^{\phi} \tag{18}$$

Then an estimate of the effective transport occurring in the multi-phase mixture $\Gamma_k^{\star}$ is obtained by applying a so-called homogenisation function which is locally dependent upon microstructure. Here, diffusion within the carbide species can be assumed negligible, so that one can define the homogenisation function by estimating a Labyrinth factor [23] which has been used to describe successfully the (generally impeding) effect of precipitates on long-range diffusion:

$$\Gamma_k^{\star} = f_{\alpha}^2 \Gamma_k^{\alpha} \tag{19}$$

where α is the continuous matrix phase (ferrite); f denotes the volume fraction. Then the flux expression Equation (16) can be rewritten as:

$$J_k = -\Gamma_k^{\star} \frac{\partial \mu_k^{l.\mathrm{eq}}}{\partial z} \tag{20}$$

where the superscript *l.eq.* has been added to emphasise that a locally-equilibrated chemical potential is assumed. The above system of equations (Equation (17)–(20)) are solved by the finite volume method (FVM) making use of flux equations derived from the discrete lattice model [24,25]. The implementation employed is described in further detail in Ref. [26].

Next, consideration is given to the prescription of the boundary condition for carbon at the scale/metal interface. The relevant chemical reactions are:

$$CO_2 = CO + 1/2O_2 \quad 2CO = CO_2 + C \tag{21}$$

A low oxygen activity controlled by the scale/metal equilibrium corresponds to a high P_{CO}/P_{CO_2} ratio, thereby producing an elevated carbon activity via the second (Boudouard) reaction. The increase of carbon content at the oxide/alloy interface expected has been described previously by defining the inward flux of carbon across the oxide/alloy interface as being proportional to the difference of the actual (reduced) time-dependent concentration at the interface ($C_C^{\star}$) and the one arising as equilibrium is fully attained (C_C^{eq}): [9], so that

$$J_C^{\star} = \alpha_C \left(C_C^{\mathrm{eq}} - C_C^{\star} \right) \tag{22}$$

To be consistent with flux expression Equation (16) derived from thermodynamic driving force, we have here rewritten Equation (22) as:

$$J_C^{\star} V_m = \alpha_{\mu,C} (\mu_C^{\mathrm{eq}} - \mu_C^{\star}) \tag{23}$$

where $\alpha_{\mu,C}$[mol m s^{-1} J^{-1}] is termed the surface reaction coefficient of carbon, thus accounting for the finite rate of its surface reaction; V_m denotes the molar volume.

Taking the oxide/alloy interface as the reference, the outward flux of metallic components (e.g. Fe, Cr and Mo) are calculated based on the predictions of oxidation kinetics described in § 3.1. Hence the migration of the oxide/alloy interface is implicitly considered. The size of the computational domain is thus decreasing during simulations. Simulations have been coupled with thermodynamic descriptions of $M_{23}C_6$ carbide, M_7C_3 carbide, HCP_A3 (M_2(C,N)) and BCC_A2 (ferrite).

3.3. Substrate penetration model (SPM)

To enable approximate calculations of carbon penetration in particular at the fin tips when 2D soft-impingement effects become important, a simplified model for carbon diffusion has proven useful. It has been termed the substrate penetration model. Assuming a rectangular cross-section of each fin which is of dimensions $L_x \times L_y$, one can estimate the diffusion field of carbon in the alloy by considering

$$\dot{C_C} = \nabla \cdot \left(D_C^{\mathrm{eff}} \nabla C_C \right) = D_C^{\mathrm{eff}} \left(\frac{\partial^2 C_C}{\partial^2 z_x} + \frac{\partial^2 C_C}{\partial^2 z_y} \right) \tag{24}$$

where D_C^{eff} is the effective chemical diffusion coefficient of carbon defined in Equation (27). In the alloy, only the concentration gradient of carbon is considered. In this case, the non-steady state carburisation described in Equation (22) can be approximated by:

$$\frac{C_C^{\star}\{t\} - C_C^{\circ}}{C_C^{\mathrm{eq}} - C_C^{\circ}} = 1 - \exp\{-\beta t\} \tag{25}$$

where C_C°, $C_C^{\star}$ and C_C^{eq} represent the initial, oxide/alloy interface and equilibrium concentration of carbon, respectively. C_C^{eq} is taken as the carbon concentration corresponding to $a_C = 1$ at different temperatures calculated from Thermo-Calc. Here β is a general 'lumped' factor describing the processes of carbon transport through the oxides, the kinetics of the Boudouard reaction [8,10] and the kinetics of carbon transport across the oxide/alloy interface [9].

Note that then one can – provided the loss of section due to oxidation is ignored – use the method of eigenfunction expansions to determine a semi-analytical solution for the carbon concentration field. It is

$$\begin{aligned} C_C\{z_x, z_y, t\} = & \sum_{n=1}^{\infty} \sum_{m=1}^{\infty} \frac{4AE\beta \left(C_C^{\circ} - C_C^{\mathrm{eq}} \right) X_n\{z_x\} Y_m\{z_y\}}{L_x L_y \left(D_C^{\mathrm{eff}} B - \beta \right)} \\ & + \left(C_C^{\mathrm{eq}} - C_C^{\circ} \right) [1 - \exp\{-\beta t\}] + C_C^{\circ} \end{aligned} \tag{26}$$

where

$$X_n\{z_x\} = \frac{\sin\{\lambda_n z_x\}}{\lambda_n}$$

$$Y_m\{z_y\} = \frac{\sin\{\lambda_m z_y\}}{\lambda_m}$$

$$\lambda_n = n\pi / L_x$$

$$\lambda_m = m\pi / L_y$$

$$A = [1 - \cos\{n\pi\}][1 - \cos\{m\pi\}]$$

$$B = \lambda_n^2 + \lambda_m^2$$

$$E = \exp\{-\beta t\} - \exp\left\{ -D_C^{\mathrm{eff}} B t \right\}$$

Diffusion in the carbides is assumed to be negligible [23]. In order to take the diffusion-blocking effect of the carbides into account, an effective diffusivity of carbon is assumed which is given by:

$$D_C^{\text{eff}} = f_\alpha^2 D_C^\alpha \tag{27}$$

where f_α and D_C^α denote the volume fraction of the ferrite and the chemical diffusion coefficient of interstitial carbon in ferrite, respectively. Without explicitly treating the phase evolution, the inhomogeneous D_C^{eff} across the spatial domain is taken as the one at the oxide/substrate interface, in this approach.

To account for the effect of oxidation on carbon penetration, the moving boundary problem can be treated – with the corner effects provided by the oxygen diffusion field ignored. Assuming a constant spinel/magnetite thickness ratio and by defining:

$$\begin{aligned} p_x &= \frac{z_x - X_{\text{sp}}\{t\}}{L_x - 2X_{\text{sp}}\{t\}} \quad p_x \in [0,1] \\ p_y &= \frac{z_y - X_{\text{sp}}\{t\}}{L_y - 2X_{\text{sp}}\{t\}} \quad p_y \in [0,1] \end{aligned} \tag{28}$$

Equation (24) can be rewritten in the following form:

$$\dot{C}_C = D_C^{\text{eff}} \frac{\partial^2 C_C}{\partial p_x^2} \left[L_x - 2X_{\text{sp}}\{t\}\right]^{-2} + D_C^{\text{eff}} \frac{\partial^2 C_C}{\partial p_y^2} \left[L_y - 2X_{\text{sp}}\{t\}\right]^{-2} \tag{29}$$

Equation (29) has been solved by using the Finite Element Solver implemented in Mathematica 11 with the boundary condition

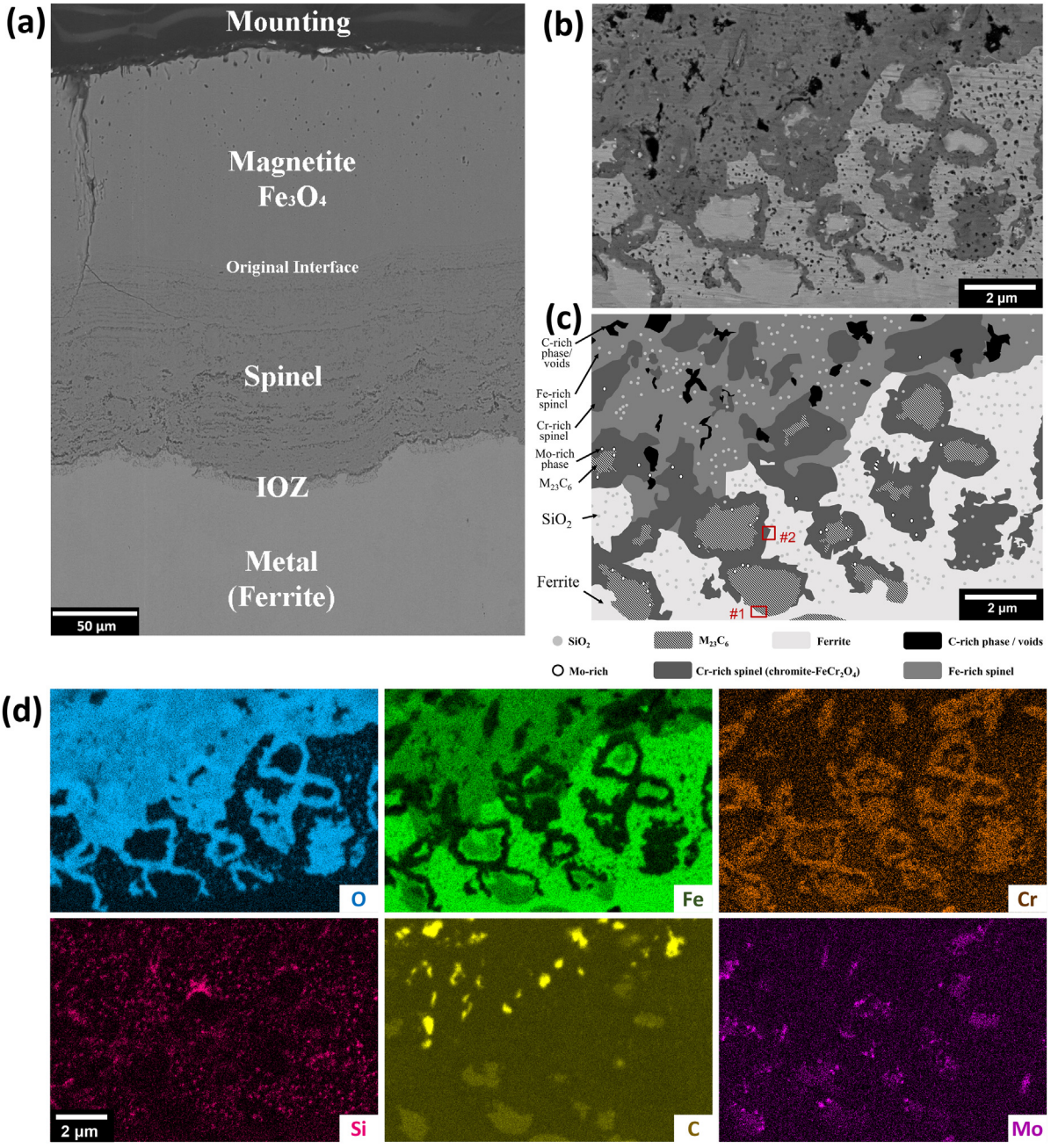

Fig. 5. (a) Backscattered SEM image of oxide cross-section showing layered structure consisting of magnetite-Fe_3O_4, banded spinel phase region and shallow IOZ; (b) Backscattered SEM and (d) EDX images of IOZ during the transition between protective/breakaway oxidation below (c) corresponding phase map with possible sites of atom probe analysis marked with red box. (For interpretation of the references to colour in this figure legend, the reader is referred to the web version of this article.)

given by Equation (25). This procedure allows the carbon diffusion field in the substrate to be estimated in 2D at minimal computational cost; in our experience this would not be possible using DicTra.

4. Experimental results

The scale microstructure developed by the steel exposed to 600 °C for ~20,000 h, at the point of breakaway, is shown in Fig. 5(a). A duplex oxide layer consisting of Fe-rich magnetite on the top and Cr-rich spinel phase at the bottom is present, and an internally oxidised zone (IOZ) between the protective scale and the substrate. Fig. 5(d) shows the results of SEM-EDX mapping across the IOZ. Detailed compositional profiling across a typical precipitate core/shell structure in the IOZ (Fig. 6(a)) is shown in Fig. 6(b); the core and the shell are identified by selected area diffractions (SAD), as shown in Fig. 6(c), as $M_{23}C_6$ carbide and $FeCr_2O_4$ chromite, respectively. The phase formation sequence, the competition between oxidation & carburisation within the IOZ, and the associated diffusion paths are discussed in detail in § 6.1.

Fig. 7(a)&(b) compare typical microstructures taken from the centre of the fin before and after exposure. Severe carburisation is evident, with large blocky $M_{23}C_6$ type carbides and needle-shape $M_2(C,N)$ being present. The $M_2(C,N)$ phase was confirmed by SAD as shown in Fig. 7(c) and TEM-EDX shown in Table 2. The variation of the measured volume fraction of carbides across the fin tip is shown in Fig. 8, and is compared with predicted carbide volume fraction corresponding to carbon activity of unity calculated from Thermo-Calc. It is seen that the measured carbide volume fraction corresponds to $a_C \sim 1$, suggesting that carbon deposition is imminent. Fig. 9(a)&(b) show a TEM image and EDX mapping taken from

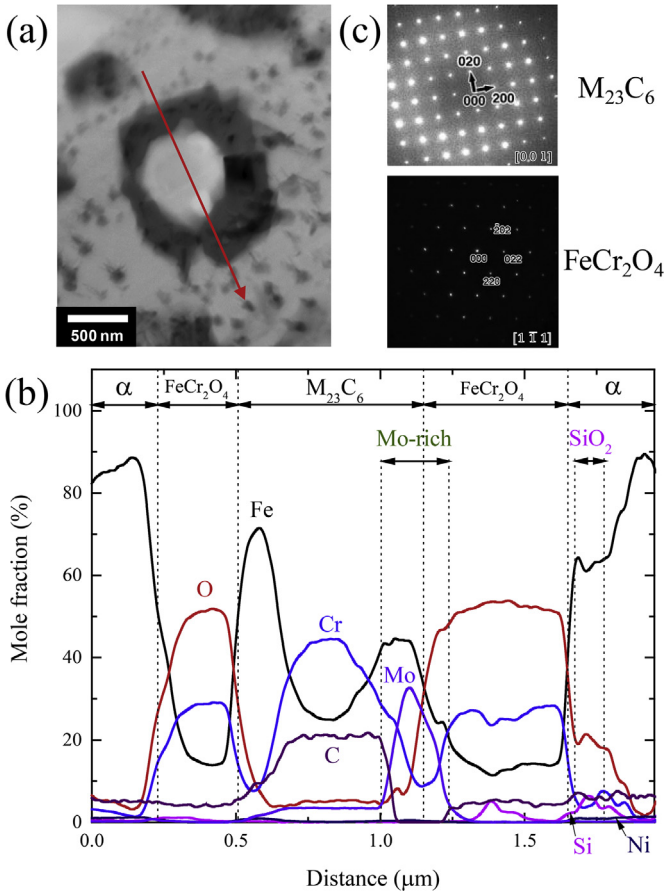

Fig. 6. (a) TEM dark field image taken from IOZ; (b) TEM-EDX line profile across the core/shell structure marked as red line in (a); (c) selected area diffraction patterns of $M_{23}C_6$ (core) and $FeCr_2O_4$ (shell).

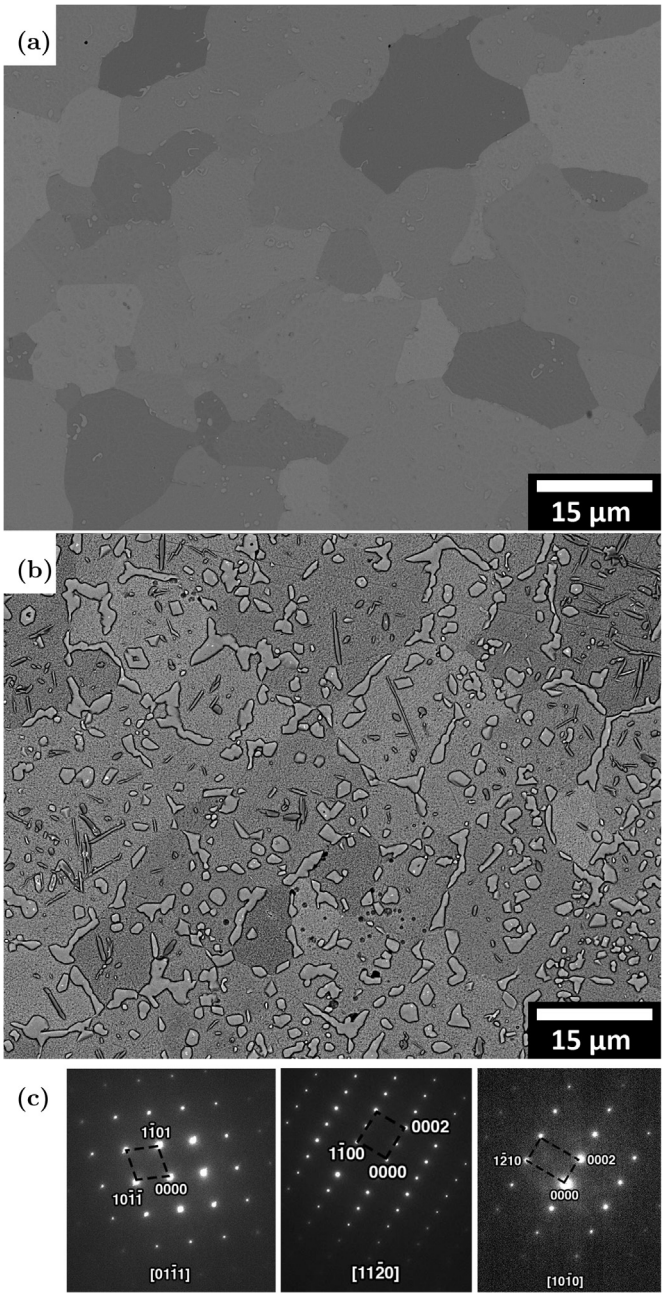

Fig. 7. Backscattered SEM images of the centre of the fin (a) before exposure and (b) at the transition between protective/breakaway oxidation during exposure, with large blocky $M_{23}C_6$ and needle shape $M_2(C,N)$; (c) selected area diffraction patterns of $M_2(C,N)$ phase present in (b).

Table 2
Chemical composition (at.%) of $M_2(C,N)$ from internal oxidised zone (IOZ) as measured by TEM-EDX.

C	Cr	Fe	Mo	N	V
24.73	61.83	0.73	1.84	10.59	0.25

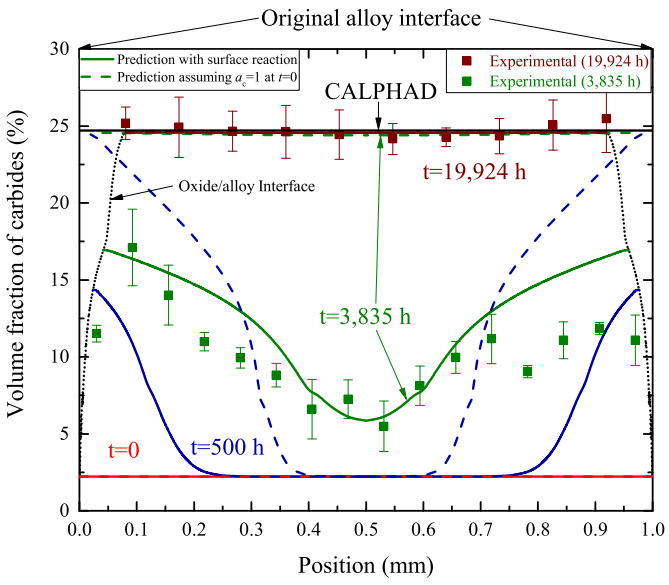

Fig. 8. Predicted profiles of volume fraction of carbides for a 1 mm fin exposed to experimental gas conditions at 600 °C at 0, 500 h, 3835 h and 19924 h, in comparison with measurements corresponding to black box marked in Fig. 1(b); simulations were conducted by 1D-DiCTra as described in § 3.2 treating migration of oxide/alloy interface and non-steady state carburisation with $\alpha_{\mu,C} = 1.2 \times 10^{-12}$ mol m s^{-1} J^{-1} (solid lines) or fixed $a_C = 1$ at the oxide/alloy interface (dashed lines).

the IOZ. Elemental carbon has been identified inside the oxide region, with its carbon mole fraction at around 95% as suggested by EDX point analysis Fig. 9(c). Fig. 9(d) shows a high-resolution TEM (HRTEM) image of oxide/graphite interface and SAD patterns taken from the graphite region. One can clearly see the layered structure of crystalline graphite with a large inter planar spacing measured to be 3.37 Å, close to the accepted basal planar spacing of graphite of 3.35 Å.

Atom probe tomography (APT) was utilised to investigate in detail the chemical compositions of the various phases observed in the IOZ. Table 3 summarises the compositions of the chromite, ferrite and $M_{23}C_6$ phases which were confirmed by APT analysis. More specifically, two interfaces including $M_{23}C_6$/ferrite and chromite/ferrite were analysed, as marked in Fig. 5(c). To enable comparisons of the degree of Cr depletion, the composition of ferrite from the fin centre is also listed in Table 3.

5. Modelling results

5.1. Oxidation kinetics

In Fig. 10, experimental measurements of oxide layer thicknesses (the dimensional metrology is detailed in Ref. [27]) are compared with the predictions of Equations (9), (14) and (15). Apparent in all the data is the approximately equal thicknesses of the outer magnetite and inner spinel layers. The inner layer occupies the space corresponding to alloy consumption as chromium in the product spinel is essentially immobile, and the equal layer thicknesses reflect the fact that the Fe/Cr ratio in the scale equals that in the alloy. During the course of this work, we have noticed a significant deviation away from purely parabolic kinetics – which can be modelled using a SiO_2 blocking factor $s = 5.2$ m^2 mol^{-1} – which we have attributed to the precipitation of this phase. Also shown are the predictions assuming $s = 0$. Predictions with $s = 5.2$ m^2 mol^{-1} show somewhat better agreement with the non-parabolic oxidation kinetics; the coefficient of determination (COD) is 0.83 for $s = 5.2$ m^2 mol^{-1} in comparison with 0.71 for $s = 0$; if this effect is not accounted for, the thicknesses are over/underpredicted at long times.

The activation energy for oxygen mobility (Q_O) and iron mobility (Q_{Fe}) deduced from the current experimental data are 276 ± 10 kJ/mol and 264 ± 11 kJ/mol respectively for s = 5.2 m^2 mol^{-1} and 255 ± 19 kJ/mol and 243 ± 18 kJ/mol respectively for s = 0. The obtained activation energies with/without considering Si effects are very close; this is due to the assumed temperature independency of the s parameter. Recent assessment [26,28] describes the P_{O_2} dependent oxygen mobility $M_O = y_{Va} y_O M_{OVa}$, where y_{Va} and y_O are equilibrium site-fractions of vacancies and oxygen ions, respectively; it gives the activation energy of M_{OVa}, $Q_{OVa} \approx 140$ kJ/mol if a reasonable oxygen vacancy formation energy is assumed [14,28–30]. Obtained from the iron tracer diffusion in magnetite, Dieckmann et al. [31] gives $Q_{Fe} = 613$ kJ/mol for the iron interstitial regime and $Q_{Fe} = -140$ kJ/mol (negative due to strong temperature dependency of defect equilibria, as discussed in Ref. [32]) for the iron vacancy regime between 900 and 1400 °C, and its extrapolation down to 500 °C is broadly consistent with measurements by Atkinson et al. [33]. At 600 °C, the tracer diffusion coefficient $D^\star = MRT$ obtained from fitting the present model to observed scaling rates shows $D^\star_O \approx 10^{-17}$ m^2/s and $D^\star_{Fe} \approx 10^{-15}$ m^2/s, compared with $D^\star_O = 2.2 \times 10^{-21}$ m^2/s [28] and $D^\star_{Fe} = 8.2 \times 10^{-18}$ m^2/s [34,35] at $P_{O_2} = 10^{-20}$ atm, interpolated from tracer diffusion experiments. The poor agreement between lattice diffusion activation energies and values found from scaling kinetics, for both oxygen and iron, indicates that mass transport in the present case is not via lattice diffusion. As proposed above, and shown schematically in the inset to Fig. 1, transport is via a combination of gas phase and oxide grain boundaries. The equal activation energies reflect the stoichiometry controlled balance of metal and oxygen fluxes, and the ongoing adjustments in boundary P_{CO_2} and microstructure which achieve it.

5.2. Carburisation kinetics

Fig. 8 shows predicted profiles of carbide fractions across the component at different times made using the 1D-DiCTra model, alongside the experimental data determined using quantitative stereology. The simulations were conducted by applying either fixed activity $a_C = 1$ at the oxide/alloy interface (dashed lines) or else the time-varying surface reaction boundary conditions as described in Equation (23) (solid lines). Clearly the assumption of a unit carbon activity at time zero leads to gross overprediction of carburisation; carbon saturation would then be expected even at times as short as 3.8 kh. Using the surface reaction boundary condition ($\alpha_{\mu,C} = 1.2 \times 10^{-12}$ mol m s^{-1} J^{-1}) gives much better agreement with the measurements; the time to carbon saturation is predicted to be close to 20 kh. These calculations demonstrate that surface-limited reaction at the oxide/alloy interface delays carbon uptake.

Fig. 11 compares the predicted evolution of carbon mole fraction (x_C) at the oxide/alloy interface and at the centre of the fin of 1 mm width for samples exposed at 600 °C, as predicted by a combination of the 1D-SPM ($\beta = 6.4 \times 10^{-8}$ s^{-1}) and 1D-DiCTra ($\alpha_{\mu,C} = 1.2 \times 10^{-12}$ mol m s^{-1} J^{-1}) models; the same oxidation kinetics model considering the SiO_2 blocking are used and loosely coupled together. The two 1D models show very close agreement except at the early stages when the effect of initial oxidation (and thus fast Fe & Cr loss from the metal) on carbon enrichment at the oxide/alloy interface is severe; this effect is obviously predicted only by 1D-DiCTra. Put another way, the DiCTra calculation predicts that when t~0, the scale-alloy interface moves extremely fast, so

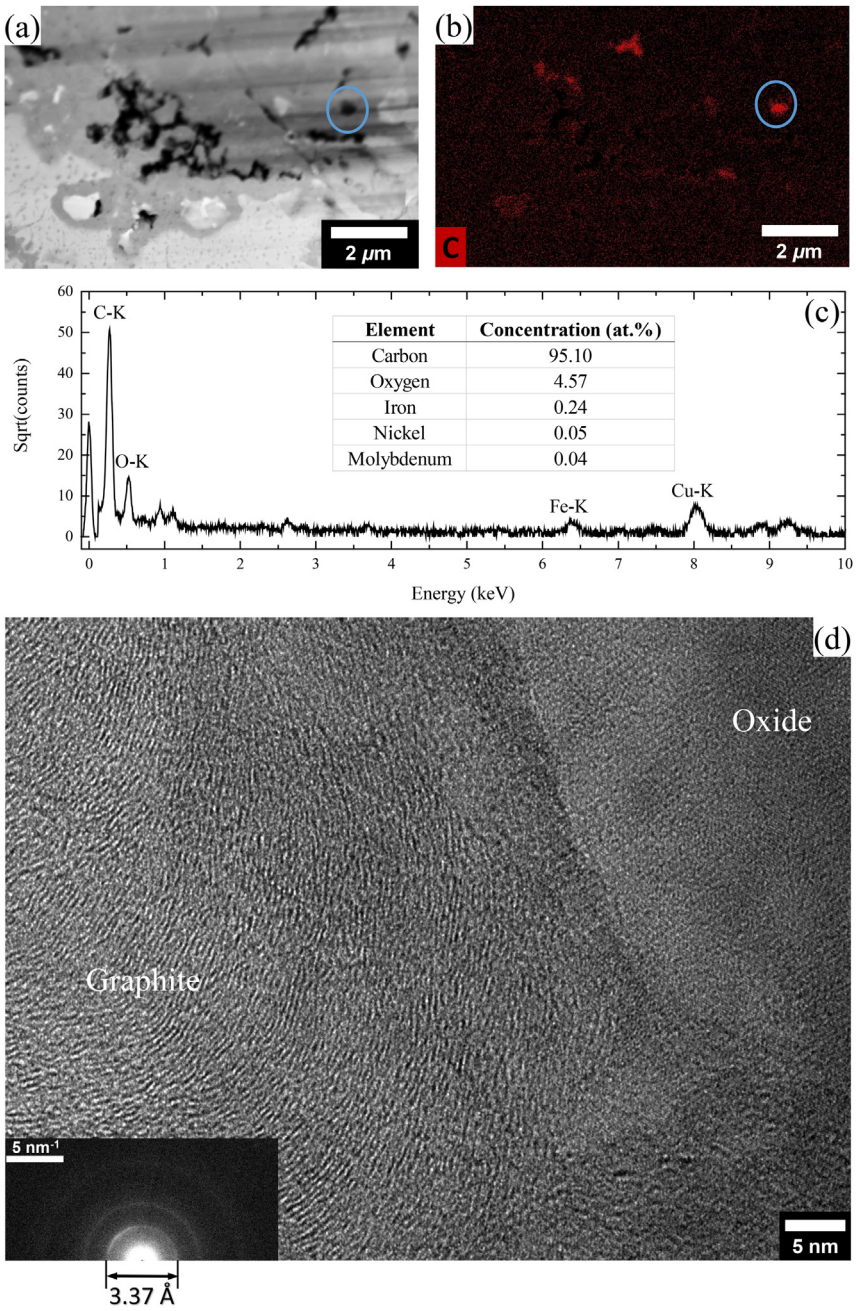

Fig. 9. (a) & (b) TEM dark field image & EDX carbon mapping taken from IOZ, respectively; (c) EDX spectrum taken from the carbon-rich region as marked in (a) & (b); (d) high-resolution TEM (HRTEM) image of oxide/graphite interface with SAD patterns of the graphite region.

rapidly that carbon cannot diffuse away from it into the metal, and is as a result concentrated at the interface. This erroneous result is an unavoidable consequence of applying a model of diffusion control to very short times, when in fact other processes slow the oxidation rate.

Note that the two 1D models show predictions of carbon saturation (provided that the appropriate pairs of $\alpha_{\mu,C}$ and β are chosen) which are consistent with each other. In particular, graphite precipitation is predicted by 1D-DiCTra after carbon saturation at around 18.8 kh; note however that such simulations are based on local-equilibrium assumptions and take no account of any energy barrier to nucleation of graphite. This will necessarily mean that the assumptions introduced are conservative with respect to graphite precipitation.

Fig. 11 reveals also a geometrical effect when one compares results from the 1D-SPM and 2D-SPM versions of the models; the 2D geometry is illustrated in Fig. 1(a) with line profiles taken across the fin tip through either the analysis point or the centre of y-axis. The 1D-SPM and 2D-SPM (centre) predictions are very close, however the 2D-SPM profile at the analysis point considered shows an acceleration of carbon ingress due to corner (soft impingement) effects.

6. Discussion

6.1. On the degradation reactions observed

Here, attack is characterised by a deep zone of internally

Table 3
Chemical composition of chromite, $M_{23}C_6$ carbide and ferrite phase from the internal oxidised zone (IOZ) as measured by atom probe tomography (at.%). The chemical composition of ferrite from the centre of the right fin is also given.

Phase	C	Co	Cr	Cu	Fe	Mn	Mo	Ni	Si	O
Chromite[#2]	0.0	0.0	27.35 ± 0.043	0.0	12.98 ± 0.088	1.36 ± 0.037	0.05 ± 0.011	0.33 ± 0.021	4.55 ± 0.071	53.36 ± 0.077
$M_{23}C_6$ [#1]	18.36 ± 0.017	0.0	29.63 ± 0.027	0.12 ± 0.002	46.38 ± 0.026	0.17 ± 0.004	4.23 ± 0.013	1.10 ± 0.011	0.01 ± 0.001	0.0
Ferrite[#2]	0.0	0.10 ± 0.001	0.0	0.15 ± 0.001	98.14 ± 0.005	0.0	0.09 ± 0.001	1.30 ± 0.004	0.0	0.0
Ferrite[#1]	0.34 ± 0.005	0.10 ± 0.005	0.80 ± 0.016	0.12 ± 0.006	97.26 ± 0.023	0.03 ± 0.003	0.22 ± 0.008	1.02 ± 0.020	0.03 ± 0.003	0.0
Ferrite[a]	0.0	0.01 ± 0.001	1.47 ± 0.004	0.12 ± 0.001	96.44 ± 0.007	0.29 ± 0.002	0.04 ± 0.001	0.15 ± 0.003	1.46 ± 0.003	0.0

[#] Analysis from the IOZ with possible sites marked in Fig. 5(c).
[a] Ferrite from the centre of the right fin.

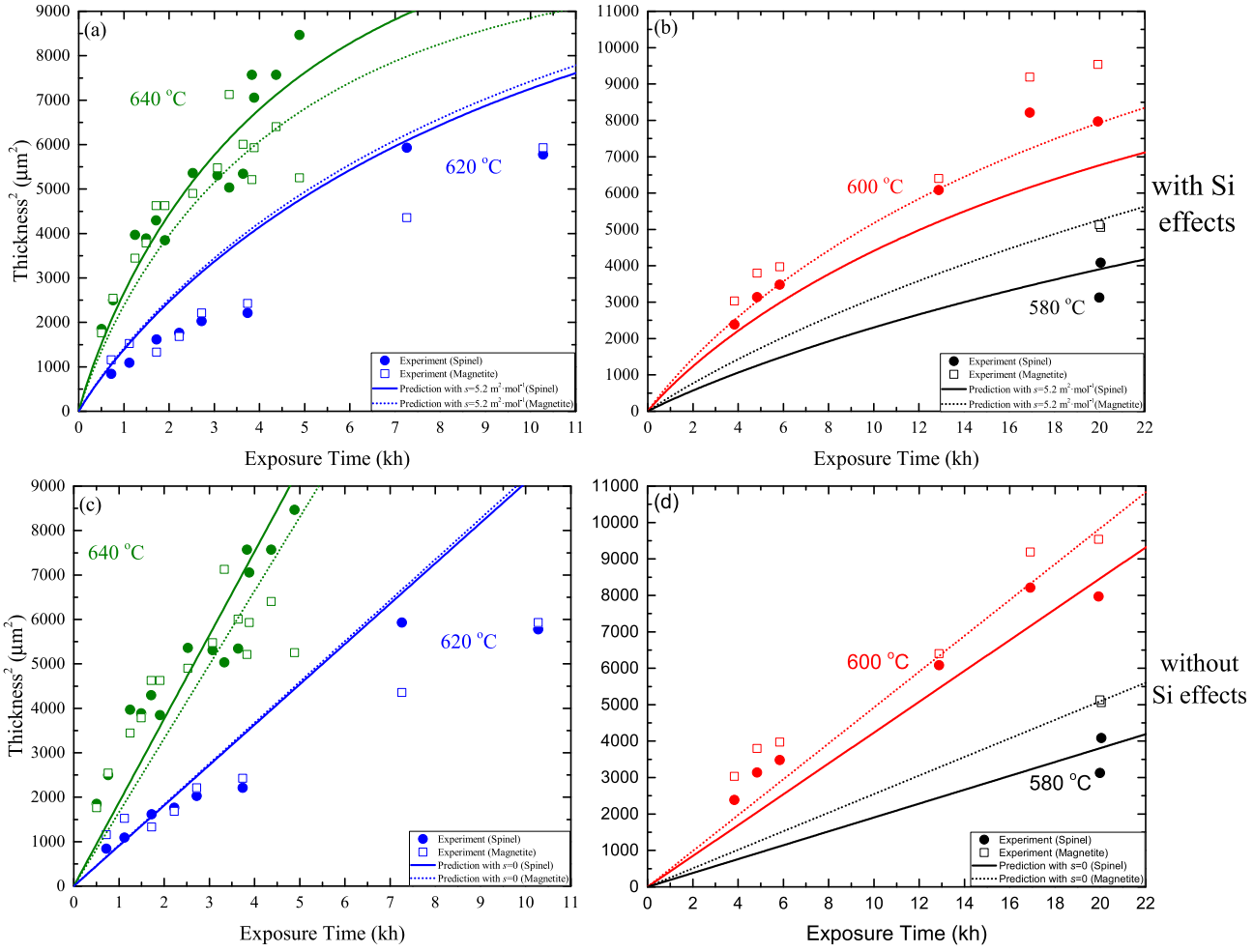

Fig. 10. Comparisons of predicted and measured thickness of spinel (solid line and solid circle) and magnetite (dash line and empty square) phase regions at (b) & (d) 580 & 600 °C and (a) & (c) 620 & 640 °C; predictions with SiO_2 blocking factor $s = 5.2$ m^2 mol^{-1} ((a) & (b)) and $s = 0$ ((c) & (d)) are compared.

precipitated Cr-rich carbides and a shallower zone containing internal oxides, principally Cr-rich chromite. There are similarities to what has been presented in Refs. [8,36]. But the reactions occurring particularly in the subsurface alloy region are complex – see Fig. 5(c). Their rationalisation is warranted.

The conventional theory for the internal precipitation within an alloy attacked by different oxidants is due to Meijering (as reviewed in Ref. [2]) and its predictions are broadly in agreement with experiment [37]. Thus the less stable precipitate is expected to be found in the deeper zone, if formed, as the more stable one is formed near the surface where both oxidant activities are at their maximum value. In the present case, the Cr-rich spinel is much more stable than the carbide, and precipitates preferentially – consistent with accepted wisdom, such that within the internal oxide zone, a_O decreases with increasing depth until its value is too low to stabilise oxide with respect to carbide. Carbon does not react within the oxide precipitation zone, but diffuses rapidly through it to reach unreacted alloy, precipitating there as Cr-rich carbide. But there are subtle differences between what is observed here and the accepted theory. In the Meijering model, the internal carbide/internal oxide interface is assumed to be the site of instantaneous conversion of carbide to oxide, the carbon solute product diffusing inward to form more carbide at a greater depth. But here, as is clear in Fig. 5(c) and from observations elsewhere [8,36,38], oxidation of the carbide takes time, and the interface is in fact somewhat diffuse implying the conversion of carbide to oxide is far from being

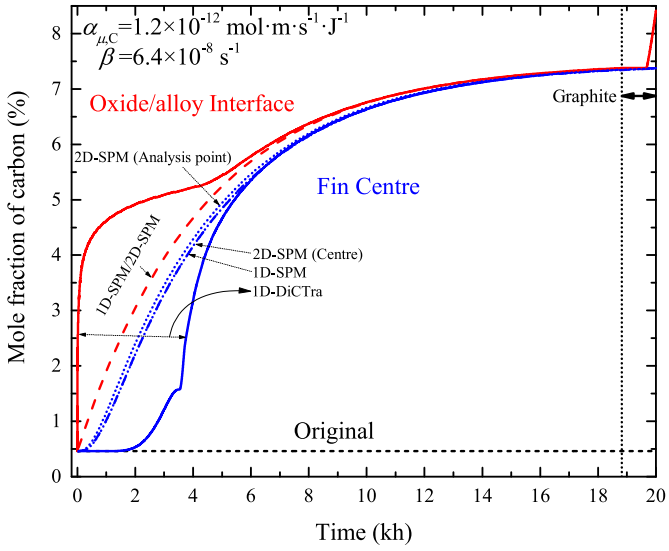

Fig. 11. Predicted evolution of carbon content at oxide/alloy interface and fin centre for a 1 mm width (6 mm long) fin exposed to experimental gas conditions at 600 °C, as predicted by 1D-DiCTra, 1D-SPM and 2D-SPM; above two carbon contents taken from the line profiles across the 2D fin tip (Fig. 1(b)) through either the analysis point or the centre of y-axis are compared.

instantaneous.

What has been observed here can be rationalised further in the following way. Within the carbide precipitation zone – which penetrates the full width of the fin – the amount of carbide varies with position (Fig. 8), as does the matrix concentration of chromium (Table 3). This is a consequence of precipitation occurring under local equilibrium conditions:

$$23\underline{Cr} + 6\underline{C} = Cr_{23}C_6 \quad (30)$$

where for simplicity the iron content has been neglected; this reaction will be governed by a solubility product K_{sp}. Thus if local equilibrium is achieved, a gradient in a_C from its maximum at the oxide-carbide interface to a minimum at the fin centre is expected, accompanied by an increase in matrix chromium concentration accounting for the observed decrease in carbide fraction.

If local equilibrium is achieved, then the locus of compositions through the reaction zone can be represented by a diffusion path on the appropriate phase diagram. Because diffusion of interstitial species is so much faster than substitutional diffusion, the latter can be neglected, and the system examined with respect to variations in a_C and a_O. Schematic diffusion paths are shown in Fig. 12 for relatively short times (t_1) and much longer times (t_2). The internal reaction product sequence of (α+$M_{23}C_6$), (α+$M_{23}C_6$+spinel), (α+SiO_2+spinel) observed in Fig. 5(c) is seen to be consistent with a diffusion path (t_1) corresponding to the expected oxygen gradient, and a carbon activity profile with its maximum in the internal oxide-internal carbide region. At longer times (t_2), carbon uptake is greater, and no single-phase ferrite remains at the centre of the fin. Furthermore, the higher carbide, Cr-rich M_2(C,N) appears, as shown on the second diffusion path. Eventually, the carbon activity will rise above unity, and graphite will precipitate, initiating breakaway.

A minor deficiency of this analysis arises from the assumption of zero metallic diffusion. In fact, chromium is locally depleted near the internal oxide, and Cr_2O_3 cannot form as would be predicted in the absence of depletion. One should note also that the predicted form of the phase diagram – particularly at low carbon and oxygen activities corresponding to the bottom left hand side of the figure – is very sensitive to the assumed levels of nitrogen in the steel. Increasing the assumed nitrogen level to 10^{-6} is enough to stabilise the (α+$M_{23}C_6$+M_2(C,N)) phase field. Since this is what is observed in the specimen centre after 20 kh exposure, it is concluded that the steel nitrogen content was of order 10^{-5}.

6.2. On the role of carbon and its treatment in numerical modelling

Carbon plays a crucial role in the breakaway phenomenon studied here, but yet various aspects of its transport behaviour remain unclear. It has been found by atom probe tomography to segregate at grain boundaries of protective Cr_2O_3 grown on an Fe-20Cr alloy carburised at 650 °C in Ar-20CO_2 at 1 atm [11]. Although

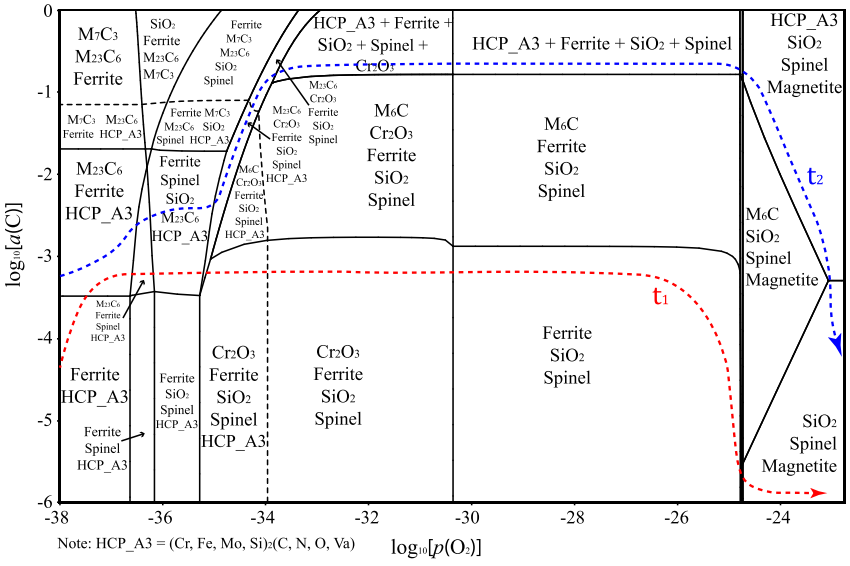

Fig. 12. Solid thermodynamic calculation predicting phase stable region at different P_{O_2} and a_C for virgin alloy with assumed molar nitrogen content of 10^{-6} at 600 °C; calculations were based on major phases included in TCFE8 and TCOX5 thermodynamic database; M_2(C, N, Va) introduced by nitrogen is predicted to present at bottom left of dashed black line, whose position is strongly dependent on nitrogen content; suggested diffusion paths for shorter times (t_1) and longer times (t_2) are marked as dashed lines.

grain boundary diffusion is indicated, the precise transport mechanism through oxide layers has not been fully established: neither the chemical form of the carbon nor its interaction with the surrounding oxide are known.

This lack of understanding justifies the approach taken here. Rather than treating the diffusion of carbon through oxide and associated mass balance at the oxide/alloy interface explicitly, the strategy for the modelling approach adopted has been to treat two semi-coupled processes, consistent with the oxide growth model (OGM) and the substrate penetration model (SPM)/DiCTra. The former focusses on the kinetics of oxidation while the latter is concerned with the penetration of carbon into the substrate, formation of internal carbides, depletion of Cr in ferrite, and graphitisation at the substrate/oxide interface.

During the protective oxidation stage there is negligible carbon present in the oxide; most carbon generated by the Boudouard reaction is injected into the alloy which acts as a carbon sink, until it is fully (super-)saturated with carbon. The volume of the sink thus determines the time required for carbon saturation (TCS); oxidation, as seen from Fig. 8, can reduce the volume of the sink by inward growth of the spinel. After the sink is fully (super-)saturated with carbon, carbon deposition and graphitisation (as predicted in Fig. 11) will alter the properties of the oxide scale by mechanical disruption and facilitate the permeation of oxidants, causing the breakaway initiations – this is described and predicted in a practical manner as the carbon saturation model in § 6.3.

It is of interest to estimate the relative contributions of oxygen and carbon to the overall mass gain observed, and their variations with temperature. This becomes possible if one assumes that any contribution to the overall weight gain by carbon is due to its uptake in the metal alone – with any contribution within the oxide scale then being assumed negligible. Fig. 13 shows predicted weight gain contributed by oxidation (by OGM) and carburisation (by SPM) at the predicted time to breakaway (predictions from § 6.3), in comparison with measured weight gain to breakaway (WGB) data. As seen, the contribution of carbon to the total weight gain is comparatively small, particularly at low temperatures with thicker oxide at the time to breakaway. It is also a constant net amount, corresponding to the amount precipitated in the steel fin, on account of the assumptions made in the modelling.

6.3. Implications for remnant life assessment

The present results provide plausible evidence that the point of breakaway initiation can be correlated with carbon saturation of the underlying substrate. Once carbon saturation is exceeded – and the necessary degree of supersaturation required for its nucleation reached – graphite (Fig. 9) can precipitate at the spinel/alloy interface. By this stage, significant Cr depletion in ferrite due to formation of Cr-rich carbides will have occurred (Table 3); the latter suppresses the formation of protective Cr-rich oxide while the former seems likely to decrease the fracture toughness of the oxide and the metal/oxide interface. Such changes in reaction morphology need to be identified if the change in the reaction kinetics accompanying breakaway is to be quantified.

Using these arguments, it becomes possible to estimate the variation of time to breakaway (TTB) with temperature by assuming – somewhat conservatively – that it corresponds to the time needed for carbon saturation (TCS). This is done in the following way. First, one identifies an analysis point (AP) close to the tip of the fin, as illustrated in Fig. 1(a), and an associated assumed mean carbon concentration at saturation, denoted X_C^{crit}. Next, for each TTB datapoint available in the experimental dataset, one solves the diffusion equation described in § 3.3, to extract a value of the parameter β, which corresponds to the lumped parameter for both the transport kinetics of carbon through oxide and the kinetics of Boudouard reaction. Then, by extrapolating β, it is possible to predict TTB at the lower operational temperatures.

Fig. 14 illustrates the predicted values of TTB against temperature along with measured data. Notice that the times to breakaway increase to very large values as the temperature falls, rising almost asymptotically as the temperature falls to the operational regime. The predicted time to breakaway initiation made with the carbon saturation model gives a higher life expectancy than that from an empirical ln{TTB}-1/T linear fitting, particularly at lower temperatures; this is more significant if a higher value of X_C^{crit} is assumed. Thus, at lower temperatures, the effect of a relatively smaller carbon diffusivity becomes more pronounced. Further future work is needed to assess the effect of any non-Arrhenius behaviour of effective carbon diffusion caused by carbide precipitation, for

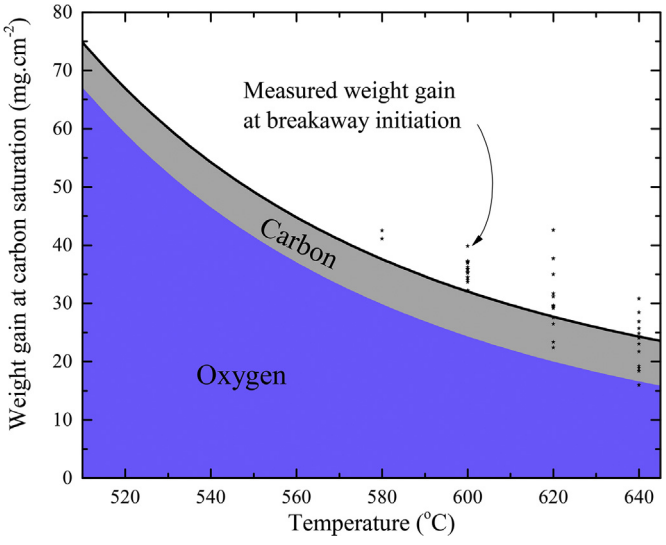

Fig. 13. Predicted weight gain contributed by oxidation and carburisation at the time of carbon saturation, in comparison with measured weight gain at breakaway (WGB) data. Note only carbon in the substrate and oxygen in the oxide scales are considered in the predictions.

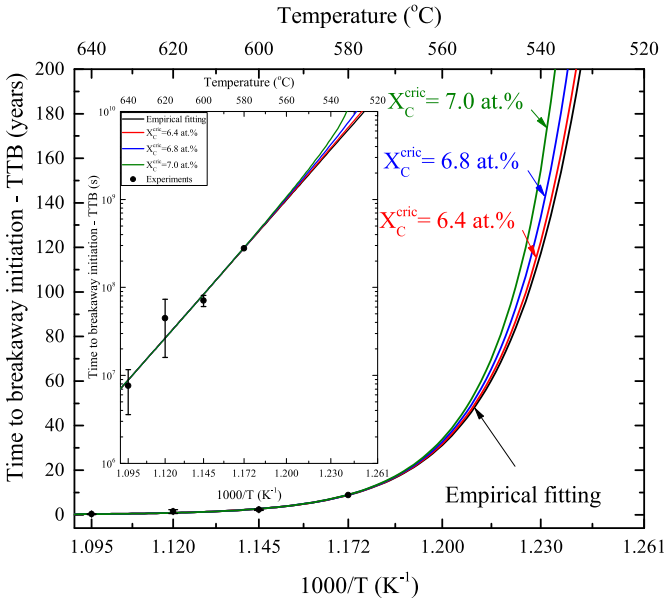

Fig. 14. Predicted time to breakaway initiation from an empirical ln{TTB}-1/T linear fitting and carbon saturation model with different carbon saturation criteria.

example by the use of a Labyrinth factor.

7. Summary & conclusions

- A 9Cr1Mo steel subjected to degradation in high pressure (42.38 bar) CO_2 at 600 °C and 20 kh has been characterised. The component contains fins of initial thickness 1 mm and length 3 mm; the evidence confirms that the substrate is saturated with respect to carbon, as indicated by measurements of the very substantial carbide precipitation and thermodynamic calculations.
- The outer oxide scale consists of an Fe-rich magnetite/spinel and Cr-rich spinel; the former contains very little Cr and grows outwards with the latter growing inwards. The presence of graphite in the inner oxide scale of spinel close to the scale/metal interface has been confirmed by transmission electron microscopy.
- Attack of the metal substrate close to the scale/metal interface – termed the internally oxidised zone (IOZ) – involves Cr-rich $M_{23}C_6$ carbide forming but becoming progressively oxidised to a Cr-rich spinel as corrosion proceeds.
- It seems plausible that carbon saturation of the substrate is a precursor to the formation of graphite, which in turn is needed for breakaway attack. This is supported by the modelling. Thus, the time for carbon saturation is shorter than that needed to cause breakaway attack.
- Nevertheless, when calculations are made using diffusion theory for the rate of carbon ingress assuming a carbon activity of unity at the metal/scale interface at time zero, the measured rate of carbon ingress is severely overpredicted. Hence it is concluded that some form of kinetically-limiting process – such as gas ingress involving the Boudouard reaction, diffusion of carbon through the outer spinel or carbon transfer across the scale-alloy interface – causes a delay to the rate of carbon penetration.
- A physically-based model is proposed for the rate of carbon uptake, which accounts for both carbon diffusion in the substrate but also the kinetically-limiting processes. By consideration of the available data for the time to breakaway oxidation at higher temperatures – which is assumed to correlate with carbon saturation of the substrate at a chosen analysis point – extrapolation to lower temperatures can be accomplished.
- The modelling allows for the relative contributions to the overall mass gain from (i) carburisation and (ii) oxidation to be estimated. The fraction of the mass gain from carburisation is approximately 1/3 under conditions of accelerated higher temperature testing but falls to substantially lower values at reactor temperatures. This is because carbon diffusion in the metal substrate starts to play a role in slowing the kinetics of attack at lower temperatures.
- The modelling presented represents a rationale for the estimation of the safe-working life of these components, and in particular extrapolation of high temperature testing to conditions more representative of operating conditions which are typically closer to 520 °C.

Acknowledgements

The authors kindly thank EDF Energy Nuclear Generation Limited, UK for the provision of funding, TGA data and experimental specimens, China Scholarship Council (CSC) for the provision of funding, Amec Foster Wheeler for the experimental support, J. Sumner and N.J. Simms (Cranfield University) for the provision of oxide dimensions. EPSRC is kindly acknowledged for financial support under the grant EP/J013501/1.

References

[1] World Nuclear News, UK Nuclear Plant Gets Ten-year Extension, 2015. http://www.world-nuclear-news.org/C-UK-nuclear-plant-gets-ten-year-extension-2001157.html [Online; accessed 28-September-2016].
[2] D.J. Young, High Temperature Oxidation and Corrosion of Metals, second ed., Elsevier, 2016.
[3] S.B. Newcomb, W.M. Stobbs, The initiation of breakaway oxidation of Fe-9Cr-1Mo in a high pressure CO_2 atmosphere, Oxid. Met. 26 (1986) 431–466.
[4] K. Kaya, S. Hayashi, S. Ukai, High-temperature oxidation behavior of 9Cr ferritic-steel in carbon dioxide, ISIJ Int. 54 (2014) 1379–1385.
[5] F. Rouillard, T. Furukawa, Corrosion of 9-12Cr ferritic-martensitic steels in high-temperature CO_2, Corros. Sci. 105 (2016) 120–132.
[6] G.B. Gibbs, L.A. Popple, Oxidation of structural-steels in CO_2 cooled reactors, Nucl. Energy J. Br. Nucl. Energy Soc. 21 (1982) 51–55.
[7] T. Gheno, D. Monceau, J. Zhang, D.J. Young, Carburisation of ferritic Fe-Cr alloys by low carbon activity gases, Corros. Sci. 53 (2011) 2767–2777.
[8] F. Rouillard, G. Moine, M. Tabarant, J. Ruiz, Corrosion of 9Cr steel in CO_2 at intermediate temperature II: mechanism of carburization, Oxid. Met. 77 (2012) 57–70.
[9] D.J. Young, P. Huczkowski, T. Olszewski, T. Hüttel, L. Singheiser, W.J. Quadakkers, Non-steady state carburisation of martensitic 9-12%Cr steels in CO_2 rich gases at 550 °C, Corros. Sci. 88 (2014) 161–169.
[10] F. Rouillard, G. Moine, L. Martinelli, J. Ruiz, Corrosion of 9Cr steel in CO_2 at intermediate temperature I: mechanism of void-induced duplex oxide formation, Oxid. Met. 77 (2012) 27–55.
[11] D.J. Young, T.D. Nguyen, P. Felfer, J. Zhang, J.M. Cairney, Penetration of protective chromia scales by carbon, Scr. Mater. 77 (2014) 29–32.
[12] K. Thompson, D. Lawrence, D. Larson, J. Olson, T. Kelly, B. Gorman, In situ site-specific specimen preparation for atom probe tomography, Ultramicroscopy 107 (2007) 131–139.
[13] E. Potter, G. Mann, in: Proc. 2nd Int. Congress Metallic Corros, NACE, New York, 1963, p. 872.
[14] F. Millot, Y. Niu, Diffusion of O^{18} in Fe_3O_4: an experimental approach to study the behavior of minority defects in oxides, J. Phys. Chem. Solids 58 (1997) 63–72.
[15] G.B. Gibbs, A model for mild steel oxidation in CO_2, Oxid. Met. 7 (1973) 173–184.
[16] J. Robertson, M.I. Manning, Criteria for formation of single layer, duplex, and breakaway scales on steels, Mater. Sci. Technol. 4 (1988) 1064–1071.
[17] M.R. Taylor, J.M. Calvert, D.G. Lees, D.B. Meadowcroft, The mechanism of corrosion of Fe-9%Cr alloys in carbon dioxide, Oxid. Met. 14 (1980) 499–516.
[18] T.D. Nguyen, J. Zhang, D.J. Young, Effects of silicon on high temperature corrosion of Fe-Cr and Fe-Cr-Ni alloys in carbon dioxide, Oxid. Met. 81 (2014) 549–574.
[19] P.C. Rowlands, D.R. Holmes, A. Whittaker, R.A. Brierley, J.C.P. Garrett, The oxidation behaviour of Fe-9Cr-1Mo steels, in: Proceedings Symposium on Gas-cooled Reactors Today, vol. 4, British Nuclear Energy Society, United Kingdom, 1983, pp. 173–181. https://inis.iaea.org/search/searchsinglerecord.aspx?recordsFor=SingleRecord&RN=15043558#.
[20] J. Fridberg, L. Torndahl, M. Hillert, Diffusion in iron, Jernkontorets Ann. 153 (1969) 263.
[21] H. Larsson, A. Engström, A homogenization approach to diffusion simulations applied to $\alpha+\gamma$ Fe-Cr-Ni diffusion couples, Acta Mater. 54 (2006) 2431–2439.
[22] H. Larsson, L. Höglund, Multiphase diffusion simulations in 1D using the DICTRA homogenization model, Calphad 33 (2009) 495–501.
[23] A. Engström, L. Höglund, J. Ågren, Computer simulation of diffusion in multiphase systems, Metall. Mater. Trans. A 25 (1994) 1127–1134.
[24] M. Hillert, The discrete lattice model for diffusion revisited, Scr. Mater. 44 (2001) 1095–1097.
[25] H. Larsson, H. Strandlund, M. Hillert, Unified treatment of Kirkendall shift and migration of phase interfaces, Acta Mater. 54 (2006) 945–951.
[26] H. Larsson, T. Jonsson, R. Naraghi, Y. Gong, R.C. Reed, J. Ågren, Oxidation of iron at 600 °C – experiments and simulations, Mater. Corros. 68 (2) (2017) 133–142, http://dx.doi.org/10.1002/maco.201508781. ISSN: 1521-4176.
[27] J. Sumner, N. Simms, A. Shin, J. Pearson, Kinetics of duplex oxide growth on 9Cr steels exposed in CO_2: application of dimensional metrology, Oxid. Met. (2017) (in press).
[28] R. Naraghi, Mobility Assessment of Fe-O System (Ph.D. thesis), KTH Royal Institute of Technology, 2017.
[29] J.E. Castle, P.L. Surman, Self-diffusion of oxygen in magnetite. Effect of anion vacancy concentration and cation distribution, J. Phys. Chem. 73 (1969) 632–634.
[30] F. Millot, J.C. Lorin, B. Klossa, Y. Niu, J.R. Tarento, Oxygen self-diffusion in Fe_3O_4: an experimental example of interactions between defects, Ber. Bunsen Ges. 101 (1997) 1351–1354. Discussion Meeting on Solute Point Defect Interactions in Crystals, Lower Saxony, Germany, Apr 07-09, 1997.
[31] R. Dieckmann, H. Schmalzried, Defects and cation diffusion in magnetite (i), Ber. Bunsenges. Phys. Chem. 81 (1977) 344–347.
[32] S. Hallström, L. Höglund, J. Ågren, Modeling of iron diffusion in the iron oxides magnetite and hematite with variable stoichiometry, Acta Mater. 59 (2011) 53–60.
[33] A. Atkinson, M.L. O'Dwyer, R.I. Taylor, ^{55}Fe diffusion in magnetite crystals at 500 °C and its relevance to oxidation of iron, J. Mater. Sci. 18 (1983)

2371–2379.
[34] R. Dieckmann, H. Schmalzried, Defects and cation diffusion in magnetite (vi): point defect relaxation and correlation in cation tracer diffusion, Ber. Bunsenges. Phys. Chem. 90 (1986) 564–575.
[35] J. Töpfer, S. Aggarwal, R. Dieckmann, Point defects and cation tracer diffusion in $(Cr_xFe_{1-x})_{3-\delta}O_4$ spinels, Solid State Ion. 81 (1995) 251–266.
[36] J. Pirón Abellán, T. Olszewski, H.J. Penkalla, G.H. Meier, L. Singheiser, W.J. Quadakkers, Scale formation mechanisms of martensitic steels in high CO_2/H_2O-containing gases simulating oxyfuel environments, Mater. High Temp. 26 (2009) 63–72.
[37] D.J. Young, S. Watson, High-temperature corrosion in mixed gas environments, Oxid. Met. 44 (1995) 239–264.
[38] T.D. Nguyen, J. Zhang, D.J. Young, Effects of cerium and manganese on corrosion of Fe-Cr and Fe-Cr-Ni alloys in Ar-20CO_2 and Ar-20CO_2-20H_2O gases at 650 °C, Corros. Sci. 100 (2015) 448–465.